



Broadened photocatalytic capability to near-infrared for CdS hybrids and positioning hydrogen evolution sites

Mengmeng Ma^{a,b}, Jun Liu^c, Huaping Zhao^d, Shizhong Yue^{a,b}, Li Zhong^{e,f}, Yanbin Huang^g, Xiaohao Jia^{a,b}, Kong Liu^{a,b}, Xiaobao Li^{e,f,*}, Zhijie Wang^{a,b,**}, Shengchun Qu^{a,b,**}, Yong Lei^{d,***}

^a Key Laboratory of Semiconductor Materials Science, Beijing Key Laboratory of Low Dimensional Semiconductor Materials and Devices, Institute of Semiconductors, Chinese Academy of Sciences, Beijing 100083, China

^b Center of Materials Science and Optoelectronics Engineering, University of Chinese Academy of Sciences, Beijing 100049, China

^c Guangdong-Hong Kong Joint Laboratory for Water Security, Engineering Research Center of Ministry of Education on Groundwater Pollution Control and Remediation, Center for Water Research, Advanced Institute of Natural Sciences, Beijing Normal University at Zhuhai, Zhuhai 519087, China

^d Fachgebiet Angewandte Nanophysik, Institut für Physik & IMN MacroNano, Technische Universität Ilmenau, Ilmenau 98693, Germany

^e School of Civil Engineering, Hefei University of Technology, Hefei 230009, China

^f Jiangsu Key Laboratory of Engineering Mechanics, Nanjing 210096, China

^g School of Mathematical Science and Engineering, Hebei University of Engineering, Handan 056038, China

ARTICLE INFO

Keywords:

Wide-spectrum light-harvesting
Hydrogen evolution reaction (HER)
Localized surface plasmon resonance (LSPR)
Directional charge transfer
Active sites

ABSTRACT

Wide-spectrum light harvesting is critical in determining practical photocatalysis water splitting. Hybridization presents a viable strategy to broaden photocatalytic capability, yet the direct conversion of near-infrared (NIR) light remains a matter of great concern. Herein, a state-of-art ternary Au nanorods@MoS₂-CdS (AMC) hybrid is designed to address this challenge. AMC achieves a leap-forward apparent quantum yield (AQY) of 1.06% at 700 nm and an AQY of 35.7% at 450 nm, extending the hydrogen evolution reaction (HER) capability of CdS hybrids to the NIR region firstly. It is revealed that the energetic hot electrons supplied by Au nanorods (NRs) are responsible for this extension. Indispensable, MoS₂ performs a platform to collect the hot electrons from Au NRs and the photoinduced electrons from CdS. The HER active sites are positioned as MoS₂-CdS interfaces both from experimental and theoretical viewpoints. This work opens up a new horizon for the forward of the wide-spectrum photocatalysis design.

1. Introduction

It is one of the high-return strategies to alleviate energy pressure by splitting water with the solar driving force and hence convert solar energy into chemical energy of hydrogen (H₂) fuel that can be stored and transported [1,2]. Configuration of an efficient photocatalyst with a broad-spectrum absorption function increasingly becomes a crucial challenge for practical photocatalysis [3]. Since most high-profile photocatalysts, such as CdS [4], are still limited to UV-visible light, hybridization with plasmonic metals presents a supportive strategy for extending the spectral response of photocatalysts without sacrificing the

electron-reducing ability [5]. Though plenty of pioneering efforts have been devoted, light utilization and energy conversion in the near-infrared (NIR) range is still rare and negligible [6–16]. What's more, separate efforts worthy of encouragement to convert NIR light to hydrogen energy achieve an unsatisfactory apparent quantum yield (AQY) at about 700 nm of less than 0.1% [6,17], which is far from practical application. For reasons, plasmonic nanometals (such as Au nanoparticles), generally possess a fast lifetime of excited electrons [18–20]. In addition, the large energy barrier in the Schottky junction with semiconductors limits the collection of low-energy electrons induced by long-wave irradiation [21].

* Corresponding author at: School of Civil Engineering, Hefei University of Technology, Hefei 230009, China.

** Corresponding authors at: Key Laboratory of Semiconductor Materials Science, Beijing Key Laboratory of Low Dimensional Semiconductor Materials and Devices, Institute of Semiconductors, Chinese Academy of Sciences, Beijing 100083, China.

*** Corresponding author.

E-mail addresses: xiaobaoli@hfut.edu.cn (X. Li), wangzj@semi.ac.cn (Z. Wang), qsc@semi.ac.cn (S. Qu), yong.lei@tu-ilmenau.de (Y. Lei).

<https://doi.org/10.1016/j.apcatb.2022.122327>

Received 10 October 2022; Received in revised form 29 November 2022; Accepted 24 December 2022

Available online 26 December 2022

0926-3373/© 2022 Elsevier B.V. All rights reserved.

How about replacing the Schottky barrier with a well-conducting electrons-collecting platform? Hydrogen evolution reaction (HER) co-catalyst, generally with good conductivity, acts as an electron and energy transport medium and provides efficient HER sites [22–25]. Thus, it is expected that charge collection and transport will be more efficient when introducing a co-catalyst into the plasmonic metal-semiconductor Schottky junction. However, questions arise. The diversity of materials and interfaces in the hybrids makes the charge transfer route complex and the active sites unintelligible. Will the improved charge transfer serve photocatalytic enhancement as expected? Where are the efficient HER sites in the ternary photocatalyst hybrids with diverse interfaces?

Here, we address the above-mentioned challenges involving NIR conversion, transfer route, and active sites toward practical photocatalyst HER by using an Au nanorods@MoS₂-CdS (AMC) ternary hybrid. First, the AMC hybrid shows a highly encouraging HER performance, with a significantly broadened light-harvesting up to the NIR region, and unprecedented AQY of 1.06% at 700 nm for the plasmonic metals involved photocatalysts and of 35.7% at 450 nm. This is the first attempt to achieve a prominent AQY in the NIR region. Second, we reveal that the energetic hot electrons from plasmonic Au nanorods (NRs) and the photoinduced electrons from CdS kinetically transfer to the MoS₂-CdS interface and are captured by water molecules. Last, we identify the exact active sites located at the MoS₂-CdS interface in the complex ternary hybrid from both experimental and theoretical aspects. This research designs a proof-of-concept ternary system where MoS₂ replaces the Schottky junction between Au NRs and CdS and provides a significant reference for the subsequent practical wide-spectrum photocatalysis.

2. Experimental section

2.1. Preparation of photocatalysts

A seed-mediated method was used to prepare Au NRs based on previous work [26]. MoS₂ nanospheres (NSs) and Au NRs@MoS₂ (AM) were formed by the hydrothermal method [27]. Herein, L-cysteine was employed as a sulfur source and a binding agent between Au and MoS₂ thanks to the Au-S bond. CdS nanoparticles (NPs) were prepared by a simple and economical PVP-assisted chemical precipitation method, where a small amount of PVP acts as the dispersant and particle spherical-shape control agent because the molecules associate with micelles. Meanwhile, this chemical precipitation progress yields almost 100% precipitation during a short period. The synthesis process of the triple AMC hybrid is shown in Fig. 1, and more details can be found in the Supporting Information. CdS adheres to the MoS₂ surface owing to

the shared S-lattice and electrostatic interaction. We also prepared ternary photocatalyst named A(P)MC replacing Au NRs with Au NPs and keeping other conditions the same for comparison.

2.2. Characterizations

The microscopic morphologies of the as-prepared photocatalysts were observed by a high-resolution transmission electron microscopy (HRTEM, JEOL, JEM-F200), along with the energy dispersive spectroscopy (EDS) element mapping being performed to analyze the element distribution of the composite catalysts. The zeta potentials and the particle size distribution of CdS and MoS₂ were determined using micro electrophoresis with a zeta potential analyzer (Beckman Coulter, DelsaNano C). X-ray diffraction (XRD) (Bruker, D8, Advance) data were collected through an X-ray powder diffractometer with Cu K α radiation ($\lambda = 0.15405$ nm, 40 kV, 40 mA). The 2θ range changed from 10° to 85° at a scanning rate of 2° min⁻¹. In-situ X-ray photoelectron spectroscopy (XPS) was conducted on a ThermoFisher escalab 250xi spectrometer equipped with a monochromatic Al K α X-ray source (1486.6 eV) operating at 100 W in the dark and under illumination from Xe lamp quipped with a 400CUT filter. The survey scans and the high-resolution scans were analyzed with a pass energy of 150 eV and 30 eV, respectively, both under vacuum ($P < 10^{-8}$ mbar). All XPS peaks have been calibrated with C1s peak (the binding energy of 284.80 eV) from adventitious carbon. A TU1950 spectrophotometer contributes to the UV-visible diffuse reflectance spectra (DRS) with an integrating sphere using BaSO₄ powder as the reference and the UV-visible absorption spectra. The UV photoelectron spectroscopy (UPS) test was carried out on the instrument ThermoFischer, ESCALAB 250Xi, and the samples were prepared by the powder compression method. Surface photovoltage spectrum (SPV) and transient photovoltage spectroscopy (TPV) were performed on CEL-TPV2000 excited by 355 nm from Beijing China Education Au-Light., Ltd. The steady-state photoluminescence (PL) and time-resolved photoluminescence (TRPL) spectra of the catalysts were performed on Edinburgh FS5 under an excitation of 365 nm. The monitoring wavelength of 477 nm in the TRPL test was selected according to the emission spectrum.

2.3. Photocatalytic H₂ evolution

All photocatalysis experiments were carried out on an automatic glass test system (Labsolar-6A, Beijing PerfectLight) equipped with a gas chromatograph (Shimadzu GC-2014). In a typical measurement, the photocatalyst powder (40 mg) was dispersed in a weak alkaline aqueous solution (100 mL) where 0.3 mol/L Na₂S and 0.3 mol/L Na₂SO₃ were



Fig. 1. Schematic illustration of AMC photocatalyst powders fabrication process.

dissolved as the sacrificial electron donor, and the suspension was ultrasonically treated for 5 min [28]. Xenon lamp equipped with filters (400 nm cutoff filter or a filter that allows 560–800 nm light to pass through) was used as the light source. The amount of H₂ evolved from the reactor was detected every half hour using the above-mentioned GC with a thermal conductivity detector (TCD). The apparent quantum yields (AQY) were estimated under the irradiation of monochromatic lights at 400, 450, 475, 500, 520, 550, 600, 650, and 700 nm to evaluate the light utilization efficiency irradiation. The AQY is evaluated according to the formula below [29]:

$$AQY = \frac{2 \times n \times N_A}{(P \times A \times t \times \lambda) / (h \times c)} \times 100\%$$

where n is the amount of substance of produced H₂, N_A is the Avogadro number, P is the power of incident light, A is the projected area of irradiation, t is the irradiation time, λ is the monochromatic wavelength, h represents the Planck constant, and c is the speed of light.

2.4. Photoelectrochemical measurements

Using an electrochemical workstation (CHI660E, Inc., Shanghai), the standard three-electrode system composed of a Pt foil as the counter electrode and Ag/AgCl (saturated KCl solution) as the reference electrode was applied for all of the photoelectrochemical measurements. FTO (fluorine-doped tin oxide, 1.5 cm × 1.5 cm) substrates coated with the photocatalyst served as the working electrode. The working electrodes were fabricated by mixing 10 mg catalysts, 1 mL absolute ethanol, and 0.1 mL Nafion. The obtained slurry was treated with continuous ultrasonic for 1 h and then was spin-coated homogeneously onto an FTO glass substrate that had been previously cleaned with DI water, acetone, isopropanol, and ethanol. The spin coating was carried out in three passes, and each 15 μ L slurry was dropped six times before spinning and in the low-speed spin coating. Each spin-coating interval is 5 min for annealing at 80 °C, with the final annealing at 80 °C for 1 h to enhance adhesion. The measurement was performed in 0.1 mol/L Na₂SO₄ solution at room temperature. A quartz cell with an all-sides window was used for external light incidence. Transient photocurrent responses were recorded at −0.6 V vs. Ag/AgCl with a program baffle controlling light on and off. Electrochemical impedance spectroscopy (EIS) was used to observe the interfacial properties of the MC, AMC, and A(P)MC with a frequency range from 0.1 MHz to 0.005 Hz. A 300 W xenon lamp (PLS-SXE300/300UV, Beijing Perfectlight) with optical filters (AM 1.5 G, a filter that allows 420 ~ 560 nm or 560 ~ 800 nm to pass, 100 mW cm^{−2}) was used as the light source to study the photoelectrochemical performance of photocatalysts at different wavelengths. The applied bias values were calculated for RHE based on the following equation:

$$E_{RHE}(V) = E_{Ag/AgCl}(V) + 0.197V + (0.059V \times pH)$$

2.5. FDTD simulation and DFT calculation

All the FDTD simulations were performed using Lumerical's FDTD Solution software. Au NRs were modeled as nanorods with a diameter of 10 nm and lengths of 36 nm and 46 nm, while Au NPs were modeled as spheres with a diameter of 50 nm. The background refractive index was set to 1.52. In this work, we performed all of the density functional theory (DFT) calculations based on first-principles employing the Vienna ab Initio Simulation Package (VASP) [30,31]. The projection augmented plane wave pseudopotential method (PAW) was used to describe the interactions between the real ions and the outer electrons, and the relaxed structures and electronic properties of all atomistic models were predicted by the local-density approximation (LDA) exchange correlation (XC) functional with Perdew-Burke-Ernzerhof (PBE) [32,33]. For all the calculations, the energy cut-off value of the plane wave expansion was set to be 450 eV. The Brillouin region was sampled

in terms of the Monkhorst pack scheme with 4 × 4 × 1 k-point grids and was scaled up or down accordingly [34]. Additionally, a vacuum space of at least 15 Å normal to the interface was set for each case to prevent the unnecessary interactions caused by artificial periodic boundary conditions. A series of atomistic models have been constructed to simulate different material systems with about 80 atoms. In the structural optimization calculations and the free energy calculations, the convergence tolerance of energy change was set as 10^{−5} eV. The convergence criterion of maximum force between atoms was fixed to 0.005 eV/Å. It is worthwhile to mention that, for the interfaces of a quantum dot, we simulated the (111) surface of Au and CdS in touch with MoS₂. The van der Waals interactions between quantum dots and MoS₂ sheet were also taken into account through a nonlocal correlation functional by including a relatively simple parametrized kernel [35]. The adsorption energy E_a for each simulation case was determined by $E_a = E_T - E_M - E_A - E_H$, where E_T is the total energy of the entire interfacial model, E_M is the total energy of pristine MoS₂, E_A is the total energy of pristine CdS (111) or Au (111), and E_H is the total energy of isolated hydrogen atom or H₂ molecule or OH molecule.

3. Results and discussion

3.1. Morphology and composition

Transmission electron microscopy (TEM) analyses are performed to gain insight into the core-shell morphology and the combination state of the hybrids. As shown in Fig. 2a, b, Au NRs are watermelon seeds-likely located inside MoS₂ NSs, which are further encapsulated well by CdS NPs with a thickness ranging from a few nanometers to a hundred nanometers. Fig. 2c gives a detailed account of the HRTEM analysis of the characteristic interplanar spacings of CdS and MoS₂, reflecting the intimate adhesion and the favorable crystallinity of these two. The grown Au NRs show good crystallinity (Fig. S1, Supporting Information), and the as-prepared MoS₂ is in the shape of monodispersed flower globose (Fig. S2a, b) with more exposed active sites [36]. CdS crystallizes into nanoparticles with a size of less than 10 nm during chemical precipitation (Fig. S2c, d). The Au NPs used for the control preparation are uniform in size with a high degree of crystallinity (Fig. S3a, b). The TEM and EDS images of the ternary composite A(P)MC photocatalyst coated with Au NPs (Fig. S3c and d) illustrate the existence of the hybrid. In addition, the Zeta potential of CdS NPs is −14.09 mV, and the positive charged MoS₂ NSs are 41.75 mV (Fig. S4) when they are dispersed in deionized water. It is thus deduced that the CdS NPs could well anchor on MoS₂ NSs, benefiting from strong electrostatic interaction and shared S-lattice [37].

XRD atlas and XPS spectrum display the crystalline, phase, and binding state of CdS and its hybrids (Fig. S5a–f). The XRD peaks of CdS appear broadened due to the quantization of the crystal particle size. The characteristic diffraction peaks of Au, MoS₂, and CdS are all clearly detected in the AMC hybrid, indicating the successful preparation of the ternary structure. In-situ XPS analysis of all kinds of components or hybrids was conducted to explore the combining situation of the components. In the meanwhile, visible-light irradiation was also commenced to help preliminarily disclose the possible charge transfer route. From Fig. S6 and Table S1, the shift of XPS peaks from sole CdS or MoS₂ to hybrids demonstrated the contribution of intense interaction and the change of electron cloud density owing to the Au-S bond and S-shared lattice. Notably, Mo elements in hybrids, whether in AM, MC, or AMC, always get a shift towards lower binding energy under visible light compared to the dark condition, indicating an increased electron cloud density [38]. Cd element shows the opposite trend. These perceptible shifts suggested the possibility that the photogenerated electrons of CdS tend to flow into MoS₂ and MoS₂ acquires hot electrons from Au NRs. In addition, the electron cloud density of MoS₂ is strongly influenced by the locally enhanced electromagnetic field of Au NRs. From in-situ XPS, we obtained significant evidence for the subsequent insight into carrier

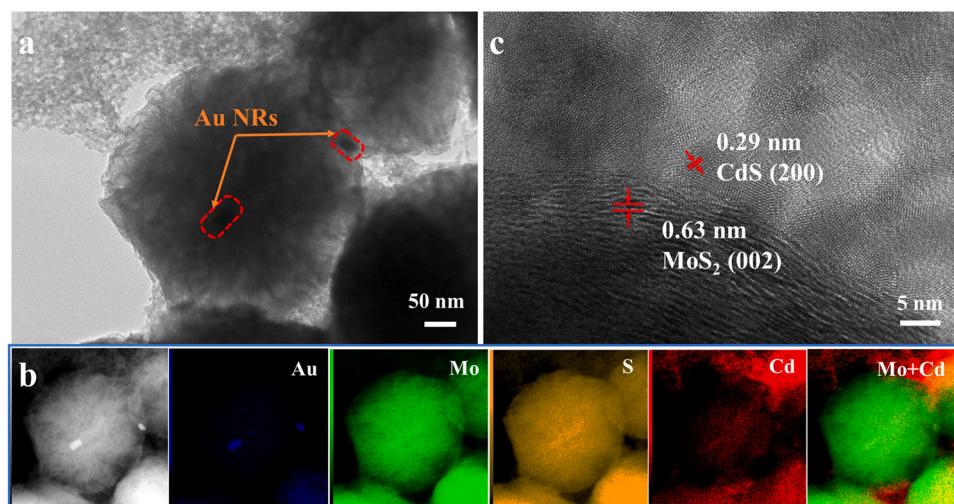


Fig. 2. (a) TEM images for AMC. (b) EDS elemental mapping images of AMC. (c) HRTEM images for AMC.

migration in complex hybrids.

3.2. Light harvesting and band structure

Fig. S7a presents Au NRs' absorption spectra with the same transversal localized surface plasmon resonance (T-LSPR) peak (~ 530 nm) and different longitudinal LSPR (L-LSPR) characteristic peaks from 668 nm to 784 nm. The red shift of L-LSPR is attributed to the increase of NRs' aspect ratio adjusted by AgNO_3 , as described in the experiment section (Supporting Information) in detail. Au NPs present a plasmon absorption peak at 530 nm (Fig. S7b). To better understand the intensified local electric field and improved absorption caused by the LSPR effect, we carried out the FDTD simulation to evaluate the spatial electric-field distribution of Au NPs and Au NRs at the different incident light wavelengths (Fig. S8) [39]. A more solid local electric field can be observed on Au NRs surfaces than on Au NPs, whether under visible or NIR irradiation, displaying Au NRs' superior light-harvesting up to the NIR region and capability for boosting HER. The diffuse reflectance spectrum (DRS) (Fig. S7c) reveals that all the CdS-based powders absorb light in the ultraviolet and blue parts of the visible region (< 550 nm) and exhibit similar absorption profiles. The only difference is the intensities with slightly moved absorption edges. The hybrids still have a considerable degree of absorption in the range out of CdS's absorption edge because of the consistent absorption of MoS_2 from 400 \sim 1000 nm (Fig. S7d). Since trace Au ($\sim 1\%$) is contained in the hybrid, rare characteristic LSPR peaks of Au are found. Even so, the promoting of Au NRs on the AMC's HER capability is not affected, which is elucidated below.

The Tauc-plots of pure CdS and MoS_2 powders (Fig. S9a and b) suggest an optical bandgap of 2.17 eV for CdS and 1.17 eV for MoS_2 . The ultraviolet photoelectron spectroscopy spectrum (UPS) (Fig. S9c and d) assesses the band edge position of the prepared CdS and MoS_2 powders, and the band structure of the ternary hybrid before contact is depicted (Fig. S10). The conduction band (CB) position of CdS is higher than the water reduction potential (-4.44 eV vs. AVS), demonstrating that HER over CdS is thermodynamic feasible. It can be judged that a Schottky barrier between Au and MoS_2 and a downward band bending from CdS's CB towards MoS_2 forms to achieve Fermi level equilibrium. These two kinds of downward band bending are kinetically conducive to the directional electrons-migration from Au or CdS to MoS_2 .

3.3. HER performance

Initially, the mass loadings of MoS_2 and Au have been optimized (Fig. S11a, b). All of the optimized ternary AMCs were prepared with a mass ratio of $w(\text{Au}): w(\text{MoS}_2): w(\text{CdS}) = 1.2: 13.8: 100$ (termed as 8%–

15% AMC, where 8% refers to the mass ratio of Au towards 100% MoS_2 in AM). 8%–15% AMCs hybrids containing trace Au NRs with different L-LSPR absorption peaks at 668, 700, 712, 753, and 784 nm are synthesized for HER performance evaluation, and an 8%–15% A(P)MC hybrid with an LSPR peak only at 530 nm is applied for comparison (named as 530 in Fig. 3a). The up-then-down tendency of the HER rate with the red-shift L-LSPR peaks is jointly determined by the LSPR effect and spectrum distribution of incident light. All of the AMCs deliver a more considerable HER performance than A(P)MC. Among them, 753 8%–15% AMC exhibits the best HER efficiency of approximately $29.6 \text{ mmol g}^{-1} \text{ h}^{-1}$ (enhanced dramatically by 412 times than pure CdS, surpassing the most reported strategies) under visible-NIR light. The remarkable efficiency difference in AMC with respect to A(P)MC should be ascribable to the fact that Au NRs can suppress inter-band damping and significantly reduce the plasmonic phase shift rate, resulting in a more prominent local field enhancement factor and relatively higher light scattering efficiency [40]. Moreover, it has been certificated that the long axis of Au NRs possesses an exciton state with a more durable lifetime than the short axis [41]. For further study of the L-LSPR effect of Au NRs, we obtained the HER rate in the NIR region (560 \sim 800 nm) of AMC hybrids (Fig. 3b), where neither CdS nor MoS_2 was able to generate H_2 . As expected, A(P)MC cannot evolve any H_2 while AMC with Au NRs behaved more or less HER capability. The most H_2 amount from 668 8%–15% AMC of $250 \mu\text{mol/g/h}$ ascribed to the matching of L-LSPR absorption range to input spectrum, and the second-best performance from 753 8%–15% AMC originated from the optimized local field enhancement factor due to the appropriate aspect ratio. Of great encouragement, our results related to the HER capability in the NIR region rank among the most satisfactory values [6,17,42–46]. It is the L-LSPR effect in Au NRs that decides the extended light-harvesting capability of CdS hybrids.

The HER tests with the changed optical power densities reveal a super-linear curve in 753 8%–15% AMC (Fig. 3c), implying the hot-electron mechanism [47]. The high optical power densities facilitate the injection of hot electrons into the adjacent semiconductor overcoming the potential barrier. Almost no super-linear relationship with optical power is found in A(P)MC, probably because the hot electrons generated by Au NPs recombine rapidly due to their short lifetime and cannot be injected into and act on the adjacent MoS_2 or CdS [4,47]. More interesting experiment results are revealed during the wavelength-dependent AQY tests (Figs. 3d, S11c). AMC achieves the highest AQY of 35.7% at 450 nm and an AQY of 1.06% at 700 nm, while the value of A(P)MC at 450 nm is only 3.83%. The H_2 yield of AMC at each wavelength is not a linear addition of AC and MC and is obviously superior to that of these two, suggesting the indispensability of both

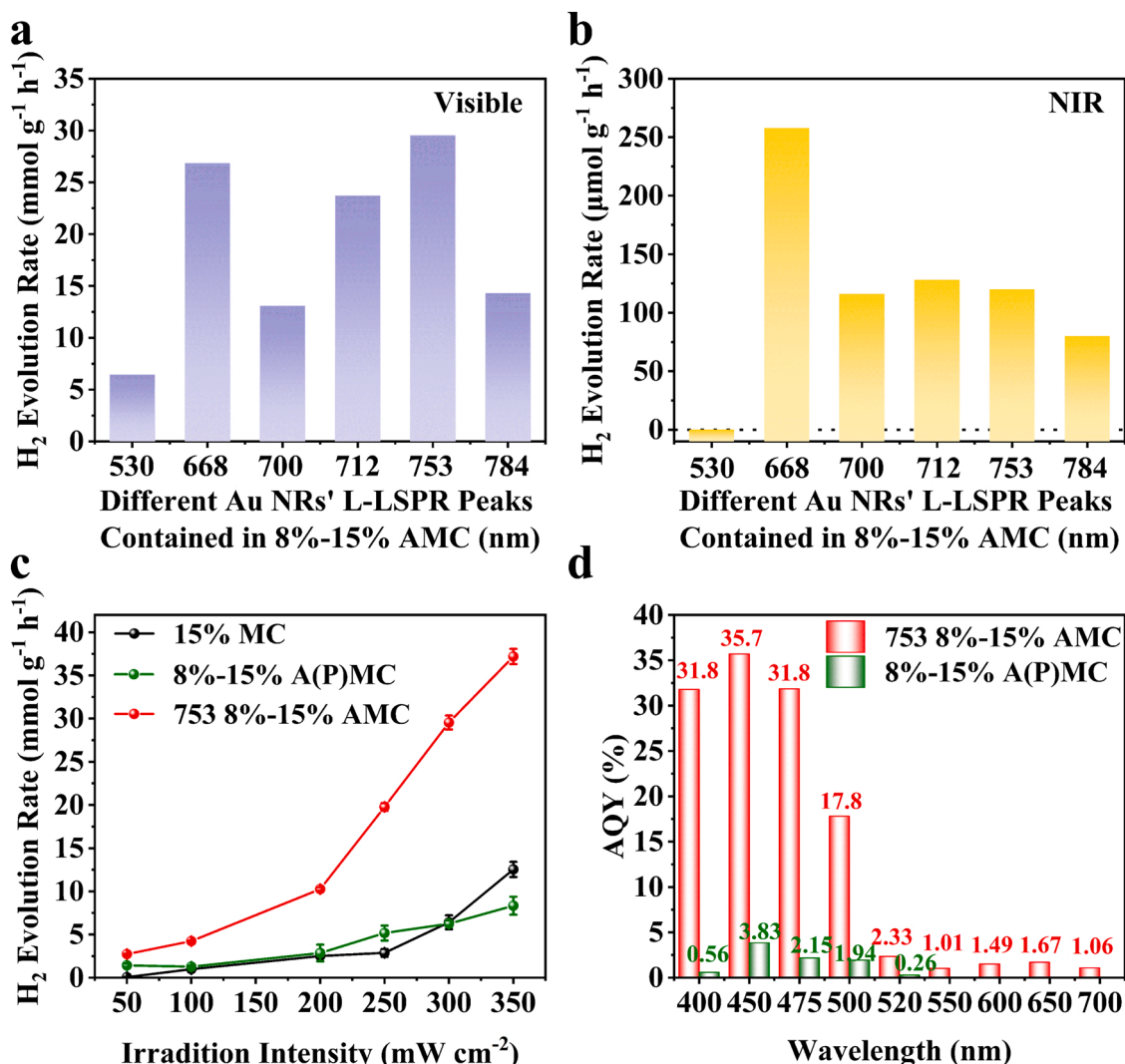


Fig. 3. HER performances of the as-prepared photocatalysts. The H₂ generation rate of 8%–15% AMCs containing Au NRs with different L-LSPR peaks and Au NPs (named as 530) under visible light irradiation (a) and NIR range (b). (c) The comparison of MC, A(P)MC, and AMC with the changed incident optical power densities. (d) The wavelength-dependent AQY of 753 8%–15% AMC and 8%–15% A(P)MC.

MoS₂ and Au NRs and the synergistic improvement of them. Unlike AMC and AC, A(P)MC cannot evolve H₂ in the region of $\lambda > 520$ nm, where CdS could not convert solar power into energized electrons and holes. These results further verify the attribution of Au NRs' L-LSPR for NIR photocatalytic capability. In the meanwhile, this enlightens us about the indispensable role of MoS₂ in the collection of hot electrons from Au NRs. Furthermore, after photocatalytic tests, the 753 8%–15% AMC photocatalyst powder was characterized in changes of structure, morphology, and combination. As presented in Fig. S12, there were no significant structural changes caused by continuous illumination, implying decent stability of the AMC hybrid's structure.

3.4. Charge separation and transport

The wavelength-dependent SPV spectra expose the directional charge transport in hybrids in Fig. 4a. For n-type CdS, SPV expresses positive surface voltage; upon being hybrid with MoS₂, the surface voltage is more positive due to the directional charge migration from CdS to MoS₂ since more photoinduced holes are left in CdS. AMC bares the most positive surface voltage, demonstrating the vivid contribution of the localized enhanced electromagnetic field of Au NRs for charge separation. The TPV relaxation curves and the increasing attenuation constants in Fig. 4b indicate the slowest charge recombination rate of

the ternary AMC hybrid [48]. PL, TRPL spectra, and electrochemical tests were also implemented to investigate the charge carrier behaviors. The fluorescence peak is confirmed and consistent with the previous report [49], while the scattering peak disappears with the excitation wavelength changed (Fig. S13a, b). Compared with the naked CdS, the binary and ternary hybrids show a noticeable fluorescence quenching effect. The TRPL lifetime of hybrids drastically declined (Fig. 4c, Table S2), demonstrating that Au NRs and MoS₂ effectively suppress the charge recombination in CdS. In addition, AMC exhibits the highest photocurrent density under the simulated solar irradiation, followed by MC and C successively (Fig. 4d), which means the most ameliorated separation efficiency of photogenerated carriers [50]. As indicated in Fig. S13c, AMC and MC show a much smaller Nyquist plot semidiameter compared to pure CdS, manifesting lower interfacial charge-transfer resistance and faster carrier migration (Table S3). The low impedance of MC should also be ascribed to the ultra-low impedance of MoS₂ (Fig. S13d). The photocurrent tests under different light regions with filters (Fig. S13e, f) further confirm the preferable photoelectric property in AMC. In the case of MC and AMC hybrids, well-conducting MoS₂ serves as a platform for electrons trapping to restrain the charge recombination on the surface of CdS [22]. Combined with the aforementioned consideration of the in-situ XPS spectra, it can be concluded that the improved charge separation is closely related to the directional

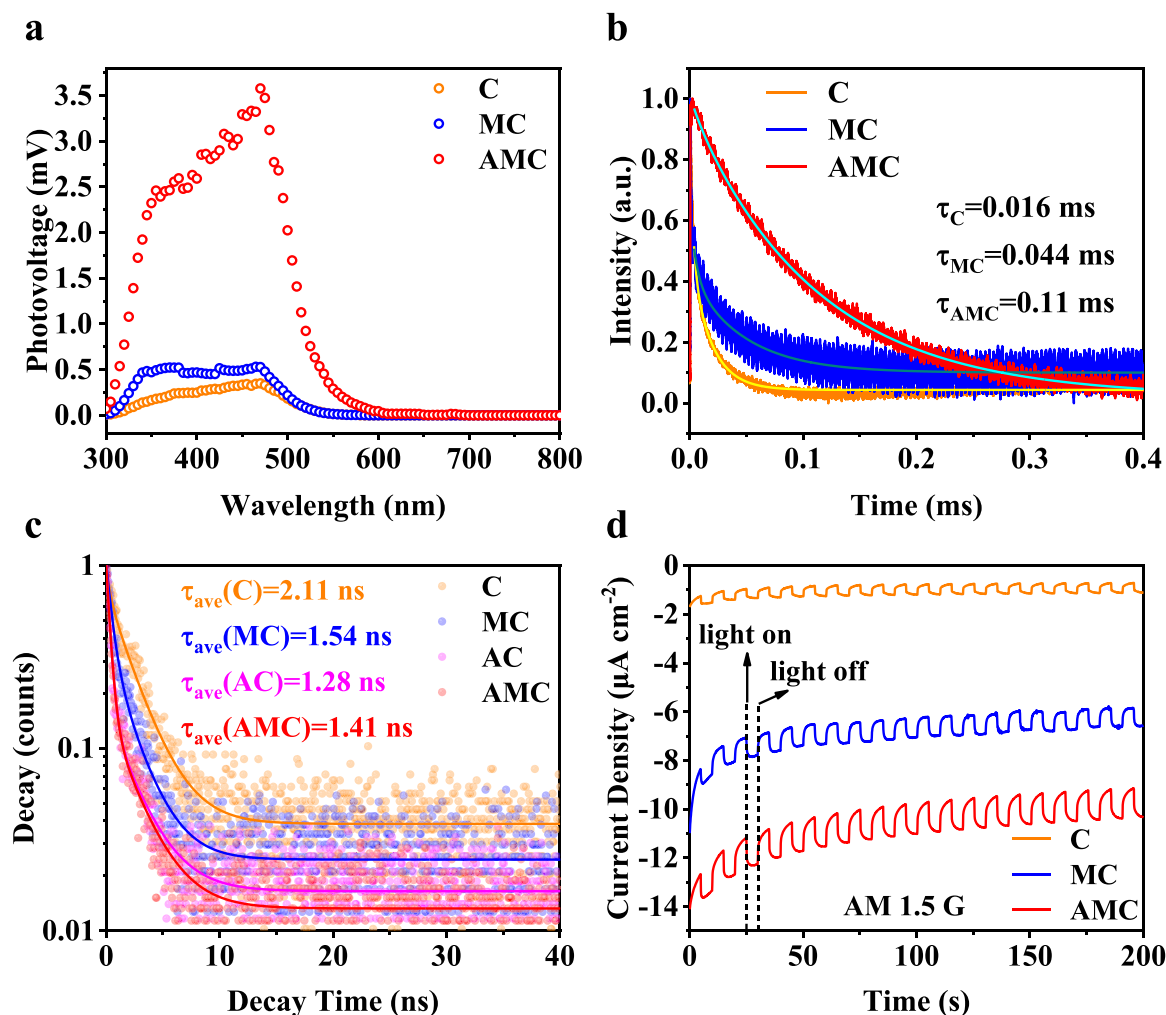


Fig. 4. (a) SPV spectrum of C, MC, and AMC. (b) TPV relaxation curves and the attenuation constants of charge recombination progress of C, MC, and AMC. (c) The TRPL spectrum and fitting lifetime of C, MC, AC, and AMC. (d) The photocurrent response curves of C, MC, and AMC under the simulated sunlight.

migration of photoinduced electrons from CdS into MoS₂, the injection of hot electrons from Au NRs to MoS₂ [51,52], and the locally enhanced electromagnetic field.

Fig. 5a displays the evaluated free energy diagrams of HER over pure C, MC, and AMC hybrids in an alkaline environment, including water adsorption, the dissociation of H₂O (H-OH), the adsorption of the proton (H⁺), and the last evolution of H₂ [53]. MC exhibits the lowest Gibbs free energy vibration of the water dissociation and the most satisfied ΔG_{H^*} (adsorption of hydrogen intermediates). These comparisons bear out that the loading of MoS₂ is conducive to the cleavage of H-OH bonds and shrinks the proton adsorption barrier, implying that MoS₂ brings considerable catalytic sites for CdS [54,55]. Nevertheless, the specific location of the catalytic sites needs to be further confirmed. It has been certified that photocatalytic activity can be ameliorated through the architecture of hybrids [56]. The ΔG_{H^*} of the AMC hybrid is larger than that of MC but closer to the ideal value of 0 than that of C. Considering AMC's best HER manifestation under actual conditions, it shows that Au does not play a role by reducing the adsorption barrier and providing HER active sites. The contribution of Au NRs is mainly from hot electrons and a locally enhanced electromagnetic field observed in the FDTD simulation [57].

The energy band structures of the components or hybrids: MoS₂, Au-MoS₂, CdS, MoS₂-CdS, and Au-CdS, are drawn in Figs. S14–S16 according to the UPS results from Fig. S9, respectively to explain their HER capability. Although MoS₂ absorbs light in the visible-NIR region and produces excited electrons, the electron in MoS₂'s CB is insufficient to

overcome the energy barrier at the MoS₂-water interface to evolve H₂. In the Au-MoS₂ hybrid, even though MoS₂ collects hot electrons from Au NRs thanks to the thermodynamically favorable Schottky junction, these electrons still end up in the same situation as pure MoS₂, as depicted in Fig. S14, where they are unable to overcome the upward potential barrier towards water. The unsatisfactory HER rate of naked CdS powders is because of the high recombination rate of photogenerated carriers observed in the PL spectrum. After being hybrid with MoS₂, a downward transfer channel of type I heterojunction opens up with an internal electric field and band offset emerging for MCs, which explains charge separation promotion. This preliminarily reflects the critical role of the MoS₂-CdS interface served as an active site since pure MoS₂ has no HER capacity. The charge density difference images (Fig. 5b) illustrate that a vigorous charge exchange occurs between CdS and MoS₂. This charge exchange is more pronounced when Au is introduced (Fig. 5c); meanwhile, electron exchange is also observed between Au and MoS₂, indicating that Au further regulates the charge transfer most likely through the localized electromagnetic field. The Density of State (DOS) calculation further validated the above conjectures about the MoS₂-CdS interface as active sites and the role of Au NRs [58]. In Fig. S17, an intermediate state around the Fermi level of CdS appears both in MC and AMC hybrids. This intermediate state (interface state) could stabilize the transferring electrons herein through the type I heterojunction. In addition, the intermediate state locates in the range of -0.94 to -0.54 eV vs. RHE, which is favorable for HER. In the AMC containing Au NRs, the electron density distribution of the intermediate state is

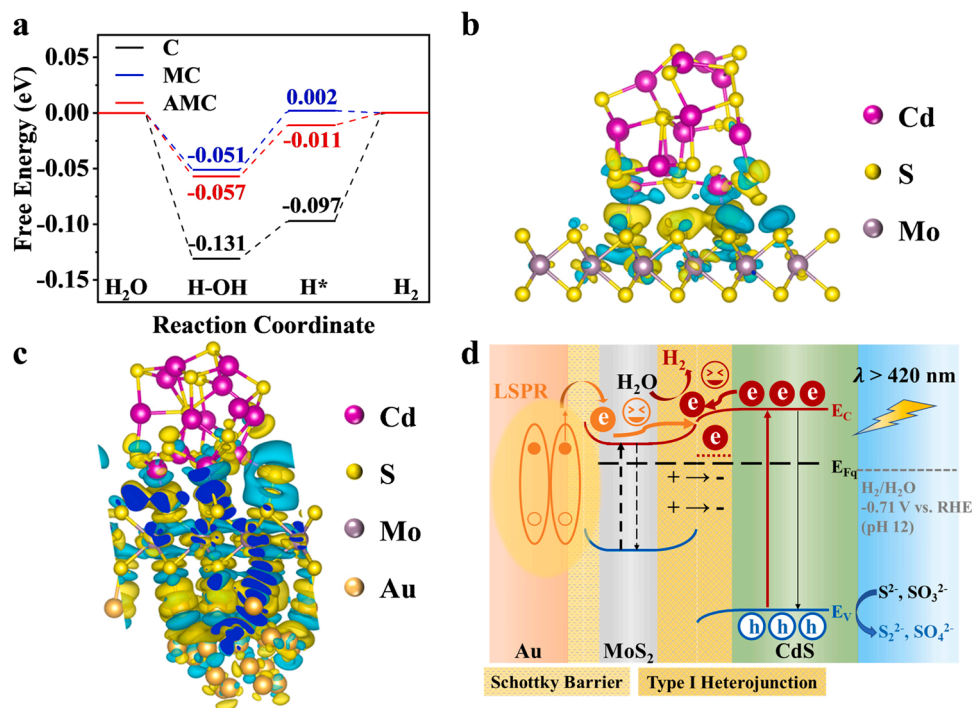


Fig. 5. (a) Free energy diagram for HER on C, MC, and AMC models. The side view of the differential charge density of (b) MC and (c) AMC. Yellow and cyan regions represent electron accumulation and depletion, respectively. (d) The charge transfer pathway for the AMC ternary system.

elevated. This demonstrates that the presence of plasmonic metals is helpful for improving the HER activity.

A plausible charge transfer pathway for the AMC ternary system is schematically proposed in Fig. 5d based on all of the above experiment results and analysis. The Schottky junction at the Au-MoS₂ interface is energetically favorable for collecting the hot electrons generated in excited Au NRs and NPs. The large difference between the work function of Au and the Fermi level of MoS₂ ensures the efficient collection of hot electrons. In particular, the hot electrons originating from the L-LSPR effect of Au NRs could be used to extend the HER activity in the NIR range where CdS cannot be excited to generate electrons. At the MoS₂-CdS interface, the small band bending due to the difference in Fermi level of 0.23 eV (Fig. S10) for the type I heterojunction possesses two positive functions. First, the excited electrons in CdS could be favorably transferred to the intermediate state at MoS₂-CdS. In this case, the loss of electrons through recombination in CdS could be prevented. Second, the electrons in MoS₂ from the excited MoS₂ and Au NRs could also be easy to overcome the low energy barrier to the intermediate state. Accordingly, the intermediate state at the MoS₂-CdS interface collects the electrons from CdS, MoS₂, and Au NRs, and the HER activity herein could be optimized. Considering the sensitivity of the photoreduction deposition of Pt nanoparticles to the active reduction sites on the photocatalyst surface, the line-scan EDS analysis of AMC after in-situ photodeposition of Pt was carried out. As shown in Fig. S18, a considerable amount of Pt element is deposited at the MoS₂-CdS interface; meanwhile, Pt nanoparticles are more prone to in-situ deposit on the surface of MoS₂ than CdS. These phenomena copiously describe the electron-accepting role of MoS₂ and the nature of the active sites at the MoS₂-CdS interface.

4. Conclusion

An ingenious design of introducing MoS₂ into the Schottky junction of the Au NRs-CdS interface is proposed. The as-prepared economical AMC exhibits impressive HER capability up to the NIR region. The enhancement factor in HER capability of AMC relative to pure CdS (412-

fold enhancement, 29.6 mmol g⁻¹ h⁻¹) in the visible-NIR region surpass the vast majority of the known modification strategies. Of significant mention is the AQY as appreciable as > 1% under NIR light. Trace Au NRs bring the integrative system energetic hot electrons for broadening HER capability, and the optimized light capture and improved charge separation as a result of the enhanced local electromagnetic field further regulate the charge migration and catalytic activity. The directional charge separation from Au or CdS to the MoS₂-CdS interface accounts for the integrally ameliorated HER performance across the full spectrum. Furthermore, we position the active sites and elucidate the underlying improvement mechanism from both the experimental and theoretical aspects. The intermediate state around CdS's Fermi level and the near-ideal ΔG_{H^+} are also evidence that the MoS₂-CdS interface serves as the final electron enrichment site and the key HER active site. This work represents the potential of CdS hybrids for practical application in wide-spectrum photocatalyst H₂ production and opens a new perspective for designing plasmon-enhanced hybrid systems.

CRediT authorship contribution statement

Mengmeng Ma: Conceptualization, Methodology, Data curation, Formal analysis, Investigation, Writing – original draft. **Jun Liu:** Formal analysis, Investigation, Methodology. **Huaping Zhao:** Formal analysis, Methodology, Writing – review & editing. **Shizhong Yue:** Data curation, Formal analysis, Methodology. **Li Zhong:** Software, Writing – original draft. **Yanbin Huang:** Formal analysis, Funding acquisition. **Xiaohao Jia:** Formal analysis. **Kong Liu:** Funding acquisition, Methodology, Project administration, Writing – review & editing. **Xiaobao Li:** Funding acquisition, Software, Writing – original draft. **Zhijie Wang:** Conceptualization, Funding acquisition, Methodology, Project administration, Supervision, Writing – review & editing. **Shengchun Qu:** Data curation, Funding acquisition, Project administration. **Yong Lei:** Conceptualization, Funding acquisition, Methodology, Project administration, Supervision, Writing – review & editing.

Declaration of Competing Interest

The authors declare that they have no known competing financial interests or personal relationships that could have appeared to influence the work reported in this paper.

Data availability

I have shared the link to my research data/code at the Attach File Step.

Acknowledgments

This work is supported mainly by the National Key Research and Development Program of China (Grant No. 2018YFE0204000), the National Natural Science Foundation of China (Grant Nos. 21975245, U20A20206, and 51972300), the Strategic Priority Research Program of the Chinese Academy of Sciences (Grant No. XDB43000000), the German Research Foundation (DFG: LE 2249/15-1) and the Sino-German Center for Research Promotion (GZ1579). Prof. K. Liu appreciates the support from Youth Innovation Promotion Association, the Chinese Academy of Sciences (No. 2020114), and the Beijing Nova Program (No. 2020117). This work is also supported by “the Fundamental Research Funds for the Central Universities of China” (Nos. PA2021KCPY0029 and LEM21A03), Jiangsu Key Laboratory of Engineering Mechanics, Southeast University (No. LEM21A03), and the National Natural Science Foundation of China (Nos. 12004094, and 32101004).

Appendix A. Supplementary information

Supplementary data associated with this article can be found in the online version at [doi:10.1016/j.apcatb.2022.122327](https://doi.org/10.1016/j.apcatb.2022.122327).

References

- [1] T. Takata, J. Jiang, Y. Sakata, M. Nakabayashi, N. Shibata, V. Nandal, K. Seki, T. Hisatomi, K. Domen, Photocatalytic water splitting with a quantum efficiency of almost unity, *Nature* 581 (2020) 411–414.
- [2] M.Q. Yang, M. Gao, M. Hong, G.W. Ho, Visible-to-NIR photon harvesting: progressive engineering of catalysts for solar-powered environmental purification and fuel production, *Adv. Mater.* 30 (2018) 1802894.
- [3] Y. Qu, X. Duan, Progress, challenge and perspective of heterogeneous photocatalysts, *Chem. Soc. Rev.* 42 (2013) 2568–2580.
- [4] J.A. Nasir, Zu Rehman, S.N.A. Shah, A. Khan, I.S. Butler, C.R.A. Catlow, Recent developments and perspectives in CdS-based photocatalysts for water splitting, *J. Mater. Chem. A* 8 (2020) 20752–20780.
- [5] J. Liu, Z. Wang, Y. Lei, A close step towards industrialized application of solar water splitting, *J. Semicond.* 41 (2020), 090401.
- [6] X. Xu, F. Luo, W. Tang, J. Hu, H. Zeng, Y. Zhou, Enriching hot electrons via NIR-photon-excited plasmon in WS₂@Cu hybrids for full-spectrum solar hydrogen evolution, *Adv. Funct. Mater.* 28 (2018) 1804055.
- [7] S. Wang, L. Tang, B. Cai, Z. Yin, Y. Li, L. Xiong, X. Kang, J. Xuan, Y. Pei, M. Zhu, Ligand modification of Au₂₅ nanoclusters for near-infrared photocatalytic oxidative functionalization, *J. Am. Chem. Soc.* 144 (2022) 3787–3792.
- [8] Z. Zheng, T. Tachikawa, T. Majima, Single-particle study of Pt-modified Au nanorods for plasmon-enhanced hydrogen generation in visible to near-infrared region, *J. Am. Chem. Soc.* 136 (2014) 6870–6873.
- [9] K. Wu, J. Chen, J.R. McBride, T. Lian, Efficient hot-electron transfer by a plasmon-induced interfacial charge-transfer transition, *Science* 349 (2015) 632–635.
- [10] M.L. Brongersma, N.J. Halas, P. Nordlander, Plasmon-induced hot carrier science and technology, *Nat. Nanotechnol.* 10 (2015) 25–34.
- [11] A.M. Valbuena-Rus, M.D. Gutiérrez-Valero, P. Arranz-Mascarós, R. López-Garzón, M. Melguizo, J. Vernet-García, M. Pérez-Mendoza, M.L. Godino-Salido, Synergy of semiconductor components of non-covalent functionalized (PdS doped)-G CdS NPs composite provide efficient photocatalytic water reduction under visible light, *Appl. Surf. Sci.* 554 (2021), 149646.
- [12] J. Xu, W.M. Yang, S.J. Huang, H. Yin, H. Zhang, P. Radjenovic, Z.L. Yang, Z. Q. Tian, J.F. Li, CdS core-Au plasmonic satellites nanostructure enhanced photocatalytic hydrogen evolution reaction, *Nano Energy* 49 (2018) 363–371.
- [13] K. Wu, W.E. Rodríguez-Córdoba, Y. Yang, T. Lian, Plasmon-induced hot electron transfer from the Au tip to CdS rod in CdS-Au nanoheterostructures, *Nano Lett.* 13 (2013) 5255–5263.
- [14] R.K. Chava, J.Y. Do, M. Kang, Smart hybridization of Au coupled CdS nanorods with few layered MoS₂ nanosheets for high performance photocatalytic hydrogen evolution reaction, *ACS Sustain. Chem. Eng.* 6 (2018) 6445–6457.
- [15] K. Chen, L. Ma, J.-H. Wang, Z.Q. Cheng, D.J. Yang, Y.Y. Li, S.J. Ding, L. Zhou, Q. Q. Wang, Integrating metallic nanoparticles of Au and Pt with MoS₂-CdS hybrids for high-efficient photocatalytic hydrogen generation via plasmon-induced electron and energy transfer, *RSC Adv.* 7 (2017) 26097–26103.
- [16] J. h Sun, B. Liu, D. Liang, M. I Zhu, X. n Peng, X. n Wang, H. Yuan, Z.J. Yang, Y. I Wang, Strategy modulation of energy transfer for the plasmon-promoted hydrogen evolution in ternary CdS-Au-MoS₂, *Int. J. Hydrog. Energy* 47 (2022) 27460–27469.
- [17] Z. Lou, S. Kim, M. Fujitsuka, X. Yang, B. Li, T. Majima, Anisotropic Ag₂S-Au triangular nanoprisms with desired configuration for plasmonic photocatalytic hydrogen generation in visible/near-infrared region, *Adv. Funct. Mater.* 28 (2018) 1706969.
- [18] J. Fang, J. Gu, Q. Liu, W. Zhang, H. Su, D. Zhang, Three-dimensional CdS/Au butterfly wing scales with hierarchical Rib structures for plasmon-enhanced photocatalytic hydrogen production, *ACS Appl. Mater. Interfaces* 10 (2018) 19649–19655.
- [19] S. Zhang, G. Chen, Z. Zhu, Y. Wang, L. Wang, S. Meng, X. Zheng, X. Fu, F. Zhang, W. Huang, S. Chen, Coordinating ultra-low content Au modified CdS with coupling selective oxidation and reduction system for improved photoexcited charge utilization, *J. Catal.* 402 (2021) 72–82.
- [20] Z. Peng, J. Zhang, P. Liu, J. Claverie, M. Sja, One-dimensional CdS/carbon/Au plasmonic nanorod photoanodes via in situ reduction-graphitization approach toward efficient solar hydrogen evolution, *ACS Appl. Mater. Interfaces* 13 (2021) 34658–34670.
- [21] X. Wang, C. Liow, D. Qi, B. Zhu, W.R. Leow, H. Wang, C. Xue, X. Chen, S. Li, Programmable photo-electrochemical hydrogen evolution based on multi-segmented CdS-Au nanorod arrays, *Adv. Mater.* 26 (2014) 3506–3512.
- [22] K. Chen, S.J. Ding, Z.J. Luo, G.M. Pan, J.H. Wang, J. Liu, L. Zhou, Q.Q. Wang, Largely enhanced photocatalytic activity of Au/XS₂/Au (X = Re, Mo) antenna-reactor hybrids: charge and energy transfer, *Nanoscale* 10 (2018) 4130–4137.
- [23] X. Zong, H. Yan, G. Wu, G. Ma, F. Wen, L. Wang, C. Li, Enhancement of photocatalytic H₂ evolution on CdS by loading MoS₂ as cocatalyst under visible light irradiation, *J. Am. Chem. Soc.* 130 (2008) 7176–7177.
- [24] X.L. Yin, L.L. Li, W.J. Jiang, Y. Zhang, X. Zhang, L.J. Wan, J.S. Hu, MoS₂/CdS nanosheets-on-nanorod heterostructure for highly efficient photocatalytic H₂ generation under visible light irradiation, *ACS Appl. Mater. Interfaces* 8 (2016) 15258–15266.
- [25] Y. Yang, Y. Zhang, Z. Fang, L. Zhang, Z. Zheng, Z. Wang, W. Feng, S. Weng, S. Zhang, P. Liu, Simultaneous realization of enhanced photoactivity and promoted photostability by multilayered MoS₂ coating on CdS nanowire structure via compact coating methodology, *ACS Appl. Mater. Interfaces* 9 (2017) 6950–6958.
- [26] H. Wei, S.K. Loeb, N.J. Halas, J.H. Kim, Plasmon-enabled degradation of organic micropollutants in water by visible-light illumination of Janus gold nanorods, *Proc. Natl. Acad. Sci. USA* 117 (2020) 15473–15481.
- [27] X. Li, S. Guo, C. Kan, J. Zhu, T. Tong, S. Ke, W.C.H. Choy, B. Wei, Au multimer@MoS₂ hybrid structures for efficient photocatalytic hydrogen production via strongly plasmonic coupling effect, *Nano Energy* 30 (2016) 549–558.
- [28] Z. Yin, M. Hu, J. Liu, H. Fu, Z. Wang, A. Tang, Tunable crystal structure of Cu–Zn–Sn–S nanocrystals for improving photocatalytic hydrogen evolution enabled by copper element regulation, *J. Semicond.* 43 (2022), 032701.
- [29] S. Guo, X. Li, J. Li, B. Wei, Boosting photocatalytic hydrogen production from water by photothermally induced biphasic systems, *Nat. Commun.* 12 (2021), 1343–1343.
- [30] N.R. Wilson, P.V. Nguyen, K. Seyler, P. Rivera, A.J. Marsden, Z.P. Laker, G. C. Constantinescu, V. Kandyba, A. Barinov, N.D. Hine, X. Xu, D.H. Cobden, Determination of band offsets, hybridization, and exciton binding in 2D semiconductor heterostructures, *Sci. Adv.* 3 (2017) 1601832.
- [31] G. Kresse, J. Furthmüller, Efficiency of ab-initio total energy calculations for metals and semiconductors using a plane-wave basis set, *Comput. Mater. Sci.* 6 (1996) 15–50.
- [32] M. Cococcioni, S. de Gironcoli, Linear response approach to the calculation of the effective interaction parameters in the LDA+U method, *Phys. Rev. B* 71 (2005), 035105.
- [33] P.E. Blöchl, Projector augmented-wave method, *Phys. Rev. B* 50 (1994) 17953–17979.
- [34] H.J. Monkhorst, J.D. Pack, Special points for Brillouin-zone integrations, *Phys. Rev. B* 13 (1976) 5188–5192.
- [35] M. Dion, H. Rydberg, E. Schröder, D.C. Langreth, B.I. Lundqvist, Van der Waals density functional for general geometries, *Phys. Rev. Lett.* 92 (2004), 246401.
- [36] B. Hinnemann, P.G. Moses, J. Bonde, K.P. Jorgensen, J.H. Nielsen, S. Hørch, I. Chorkendorff, J.K. Nørskov, Biomimetic hydrogen evolution: MoS₂ nanoparticles as catalyst for hydrogen evolution, *J. Am. Chem. Soc.* 127 (2005) 5308–5309.
- [37] X.Y. Liu, H. Chen, R. Wang, Y. Shang, Q. Zhang, W. Li, G. Zhang, J. Su, C.T. Dinh, F. P.G. de Arquer, J. Li, J. Jiang, Q. Mi, R. Si, X. Li, Y. Sun, Y.T. Long, H. Tian, E. H. Sargent, Z. Ning, 0D–2D quantum dot: metal dichalcogenide nanocomposite photocatalyst achieves efficient hydrogen generation, *Adv. Mater.* 29 (2017) 1605646.
- [38] Y. Yang, M. Faheem, L. Wang, Q. Meng, H. Sha, N. Yang, Y. Yuan, G. Zhu, Surface pore engineering of covalent organic frameworks for ammonia capture through synergistic multivariate and open metal site approaches, *ACS Cent. Sci.* 4 (2018) 748–754.

- [39] Y. Huang, J. Liu, C. Zhao, X. Jia, M. Ma, Y. Qian, C. Yang, K. Liu, F. Tan, Z. Wang, X. Li, S. Qu, Z. Wang, Facile synthesis of defect-modified thin-layered and porous g-C₃N₄ with synergetic improvement for photocatalytic H₂ production, *ACS Appl. Mater. Interfaces* 12 (2020) 52603–52614.
- [40] J. Zhang, M. Li, Y. He, X. Zhang, Z. Cui, P. Fu, M. Liu, X. Qiao, Q. Zhao, X. Pang, From 0-dimension to 1-dimensions: Au nanocrystals as versatile plasmonic photocatalyst for broadband light induced RAFT polymerization, *Polym. Chem.* 12 (2021) 2439–2446.
- [41] Y. Si, S. Cao, Z. Wu, Y. Ji, Y. Mi, X. Wu, X. Liu, L. Piao, What is the predominant electron transfer process for Au NRs/TiO₂ nanodumbbell heterostructure under sunlight irradiation? *Appl. Catal. B Environ.* 220 (2018) 471–476.
- [42] W. Jiang, S. Bai, L. Wang, X. Wang, L. Yang, Y. Li, D. Liu, X. Wang, Z. Li, J. Jiang, Y. Xiong, Integration of multiple plasmonic and co-catalyst nanostructures on TiO₂ nanosheets for visible-near-infrared photocatalytic hydrogen evolution, *Small* 12 (2016) 1640–1648.
- [43] C. Han, Q. Quan, H.M. Chen, Y. Sun, Y.-J. Xu, Progressive design of plasmonic metal–semiconductor ensemble toward regulated charge flow and improved Vis–NIR-driven solar-to-chemical conversion, *Small* 13 (2017) 1602947.
- [44] W. Feng, L. Zhang, Y. Zhang, Y. Yang, Z. Fang, B. Wang, S. Zhang, P. Liu, Near-infrared-activated NaYF₄:Yb³⁺, Er³⁺/Au/CdS for H₂ production via photoreforming of bio-ethanol: plasmonic Au as light nanoantenna, energy relay, electron sink and co-catalyst, *J. Mater. Chem. A* 5 (2017) 10311–10320.
- [45] M. Zhu, X. Cai, M. Fujitsuka, J. Zhang, T. Majima, Au/La₂Ti₂O₇ nanostructures sensitized with black phosphorus for plasmon-enhanced photocatalytic hydrogen production in visible and near-infrared light, *Angew. Chem. Int. Ed.* 56 (2017) 2064–2068.
- [46] X. Cai, M. Zhu, O.A. Elbanna, M. Fujitsuka, S. Kim, L. Mao, J. Zhang, T. Majima, Au nanorod photosensitized La₂Ti₂O₇ nanosteps: successive surface heterojunctions boosting visible to near-infrared photocatalytic H₂ evolution, *ACS Catal.* 8 (2017) 122–131.
- [47] B.T. Zhang, J. Liu, S. Yue, Y. Teng, Z. Wang, X. Li, S. Qu, Z. Wang, Hot electron injection: an efficacious approach to charge LaCoO₃ for improving the water splitting efficiency, *Appl. Catal. B Environ.* 219 (2017) 432–438.
- [48] Q. Chen, Y. Liu, X. Gu, D. Li, D. Zhang, D. Zhang, H. Huang, B. Mao, Z. Kang, W. Shi, Carbon dots mediated charge sinking effect for boosting hydrogen evolution in Cu-In-Zn-S QDs/MoS₂ photocatalysts, *Appl. Catal. B Environ.* 301 (2022), 120755.
- [49] G. Yu, X. Wang, J. Cao, S. Wu, W. Yan, G. Liu, Plasmonic Au nanoparticles embedding enhances the activity and stability of CdS for photocatalytic hydrogen evolution, *Chem. Commun.* 52 (2016) 2394–2397.
- [50] A. Liao, H. He, Y. Zhou, Z. Zou, Typical strategies to facilitate charge transfer for enhanced oxygen evolution reaction: case studies on hematite, *J. Semicond.* 41 (2020), 091709.
- [51] Y. Shi, J. Wang, C. Wang, T.T. Zhai, W.J. Bao, J.J. Xu, X.H. Xia, H.Y. Chen, Hot electron of Au nanorods activates the electrocatalysis of hydrogen evolution on MoS₂ nanosheets, *J. Am. Chem. Soc.* 137 (2015) 7365–7370.
- [52] Z. Li, Y. Xiao, Y. Gong, Z. Wang, Y. Kang, S. Zu, P.M. Ajayan, P. Nordlander, Z. Fang, Active light control of the MoS₂ monolayer exciton binding energy, *ACS Nano* 9 (2015) 10158–10164.
- [53] B. Zhang, J. Hou, Y. Wu, S. Cao, Z. Li, X. Nie, Z. Gao, L. Sun, Tailoring active sites in mesoporous defect-rich NC/V_o-WON heterostructure array for superior electrocatalytic hydrogen evolution, *Adv. Energy Mater.* 9 (2019) 1803693.
- [54] X. Han, G. He, Y. He, J. Zhang, X. Zheng, L. Li, C. Zhong, W. Hu, Y. Deng, T.Y. Ma, Engineering catalytic active sites on cobalt oxide surface for enhanced oxygen electrocatalysis, *Adv. Energy Mater.* 8 (2018) 1702222.
- [55] H. Yan, Y. Xie, Y. Jiao, A. Wu, C. Tian, X. Zhang, L. Wang, H. Fu, Holey reduced graphene oxide coupled with an Mo₂N–Mo₂C heterojunction for efficient hydrogen evolution, *Adv. Mater.* 30 (2018) 1704156.
- [56] H. Zeng, Z. Li, G. Li, X. Cui, M. Jin, T. Xie, L. Liu, M. Jiang, X. Zhong, Y. Zhang, H. Zhang, K. Ba, Z. Yan, Y. Wang, S. Song, K. Huang, S. Feng, Interfacial engineering of TiO₂/Ti₃C₂ MXene/carbon nitride hybrids boosting charge transfer for efficient photocatalytic hydrogen evolution, *Adv. Energy Mater.* 12 (2022) 2102765.
- [57] M. Ma, Y. Huang, J. Liu, K. Liu, Z. Wang, C. Zhao, S. Qu, Z. Wang, Engineering the photoelectrochemical behaviors of ZnO for efficient solar water splitting, *J. Semicond.* 41 (2020), 091702.
- [58] S. Wang, Y. Gao, S. Miao, T. Liu, L. Mu, R. Li, F. Fan, C. Li, Positioning the water oxidation reaction sites in plasmonic photocatalysts, *J. Am. Chem. Soc.* 139 (2017) 11771–11778.